10-8-2024

Closed-loop Adaptive Optics in the Presence of Speckle and Weak Scintillation

Derek J. Burrell
University of Arizona

Mark F. Spencer
Air Force Institute of Technology

Ronald G. Driggers
University of Arizona

Recommended Citation

Burrell, D. J., Spencer, M. F., & Driggers, R. G. (2024). Closed-loop adaptive optics in the presence of speckle and weak scintillation. Journal of Optics, 26(11), 115608. https://doi.org/10.1088/2040-8986/ad7f67

Closed-loop adaptive optics in the presence of speckle and weak scintillation

OPEN ACCESS
IOP Publishing
Journal of Optics
J. Opt. **26** (2024) 115608 (14pp)
https://doi.org/10.1088/2040-8986/ad7f67

Closed-loop adaptive optics in the presence of speckle and weak scintillation

Derek J Burrell[1,*], **Mark F Spencer**[2] **and Ronald G Driggers**[1]

[1] The University of Arizona, Wyant College of Optical Sciences, 1630 E University Boulevard, Tucson, AZ 85721, United States of America
[2] Air Force Institute of Technology, Department of Engineering Physics, 2950 Hobson Way, Dayton, OH 45433, United States of America

E-mail: derekburrell@optics.arizona.edu, mark.spencer@osamember.org and rdriggers@optics.arizona.edu

Received 29 July 2024, revised 16 September 2024
Accepted for publication 25 September 2024
Published 8 October 2024

Abstract
In this paper, we show that speckle averaging helps to improve adaptive-optics (AO) performance in closed loop as a result of reduced measurement error associated with a Shack–Hartmann wavefront sensor (SHWFS); however, this reduction is rendered ineffective with increasing beacon anisoplanatism. We do so operating in a weak-scintillation regime, where the SHWFS offers robust performance, and using in-plane translation of the illuminated rough surface to accomplish frame-to-frame speckle diversity. Understanding these trade-space limitations is critical when performing AO with non-cooperative, extended-source beacons.

Keywords: atmospheric turbulence, beacon anisoplanatism, rough surface scattering, speckle phenomena, adaptive optics, wavefront sensing

1. Introduction

For applications involving adaptive optics (AO), a beacon provides a reference wave for measurement and reconstruction. In astronomical applications, for example, natural guide stars or laser guide stars serve as distant, point-source-like beacons that sample the atmosphere with high fidelity [1]. In non-cooperative directed energy applications, however, the only option is to create an extended beacon on the object being imaged and tracked. Such a beacon manifests from the scattering of coherent illumination from an optically rough surface on the object. In turn, extended beacons give rise to speckle and anisoplanatism—phenomena that compromise the closed-loop performance of an AO system.

Speckle is an interference phenomenon arising from coherent illumination that scatters from an optically rough surface in the object plane. Upon propagation to a pupil plane, the backscattered illumination self-interferes to form bright and dark patches individually known as 'speckles.' Assuming quasi-monochromatic illumination, linear polarization, and surface-height variations that exceed half the optical wavelength, the speckle pattern becomes 'fully developed' with contrast going to unity. In non-cooperative directed energy applications, speckle acts as multiplicative noise with deleterious effects on image quality [2] and track quality [3].

Given an extended beacon, the AO system must sense and correct for atmosphere-induced phase aberrations (resulting in scintillation) separately from object-induced phase aberrations (resulting in speckle). However, what the wavefront sensor (within the AO system) actually measures and reconstructs is a sum of path-integrated contributions from both sources of phase aberration. The Shack–Hartmann wavefront sensor (SHWFS), for example, uses individual lenslets to divide the receiver aperture into subapertures that sample the incoming wavefront and focus the samples onto a detector array. The

* Author to whom any correspondence should be addressed.

relative centroid positions of these focused spots correspond to local tilts (a.k.a. phase gradients) present in each subaperture. Accordingly, we can use the centroid measurements to reconstruct a pupil-plane phase function that estimates the path-integrated phase aberrations resulting from atmospheric turbulence. A predistorting optic, such as a continuous-facesheet deformable mirror (DM), can then apply this pupil-plane phase function on an outgoing laser beam, so that it focuses to an aimpoint in the object plane. We then repeat this process in a null-seeking control loop so that the measured and reconstructed wavefront error goes to zero.

Subaperture to subaperture, the presence of speckle also means that the SHWFS collects and resolves nonuniform irradiance in the pupil and image planes, respectively. Since the centroid represents an irradiance-weighted center of mass, these irradiance fades skew the wavefront measurement even further. Thus, we must mitigate the effects of speckle—both the object-induced phase aberrations and the object-induced irradiance fades—to obtain good closed-loop performance.

One way to mitigate the effects of speckle is to perform speckle averaging. In so doing, it is common to assume that frame-to-frame speckle decorrelates at a faster rate than the scintillation. This assumption can be a sound one given dynamically vibrating objects, but at high frame rates it is possible that speckle only partially decorrelates between observations. Although we require more frames with partially correlated than with fully uncorrelated speckle to achieve the same effect, sufficient energy accumulation in either case effectively averages out unwanted speckle noise.

Despite the benefits of speckle averaging, there are limitations to keep in mind regarding its effectiveness. For one, fast framing is required of the focal plane array (FPA) for the most effective speckle averaging—a limitation we will explore in more detail in the analysis that follows. Another limitation stems from the presence of beacon anisoplanatism.

Anisoplanatism is a shift-varying phenomenon that results from an extended source and distributed-volume phase aberrations. As shown in figure 1, we can use a Huygens–Fresnel description of the problem and break the extended source (associated with the extended beacon) up into a bunch of point sources. We can then add up their contributions after propagation to a plane of interest. If the phase aberrations distribute themselves along the propagation path, a point source on one end of the extended source will experience a different set of phase aberrations compared with a point source on the other end of the extended source. Nonetheless, the wavefront sensor (within the AO system) will measure and reconstruct the contributions from all the point sources within the extended source [4]. This so-called 'path averaging' leads to degraded AO performance when focusing an outgoing laser beam to an aimpoint in the object plane. Put simply, the path-integrated phase aberrations experienced by the extended beacon will not be the same as the path-integrated phase aberrations experienced by the focused laser beam. As such, we will also explore the limitations of beacon anisoplanatism in the analysis that follows.

In this paper, we model extended beacons of various sizes using plane-wave illumination of optically rough square objects[3]. We assume varying degrees of speckle correlation from one frame to the next, up to and including total decorrelation. We also assume that there is potential for beacon anisoplanatism when the beacon size exceeds that of the isoplanatic patch. We then model horizontal-path propagation with Kolmogorov turbulence and frozen flow through wave-optics simulations. Finally, we model a closed-loop AO system.

In our approach, we characterize the severity of the speckle and anisoplanatism using the object Fresnel number and object angular extent relative to the isoplanatic angle, respectively. It is important to note that the degree of speckle correlation between frames plays a significant role in our ability to perform speckle averaging [5, 6]; thus, truly uncorrelated speckle comprises a 'best-case scenario' in the sense that it draws independent and identically distributed (i.i.d.) speckle data from one frame to the next. In addition to this limiting case, we explore the cases of 25%, 50%, 75% and 100% speckle decorrelation between consecutive frames by simulating dynamic speckle with high fidelity.

Dynamic speckle averaging represents just one possible solution to the speckle-mitigation problem, of which several others exist [7]. Such methods generally impose some condition of partial coherence or polarization. For example, we could reduce the spatial coherence of our illumination using dynamic diffusers [8], multimode waveguides [9], DMs [10], or tiled apertures [11]. Similarly, we could reduce the temporal coherence of our illumination via spectral-linewidth broadening [12–16]. The coherence and polarization trade space is rich with potential ideas [17]. Dynamic speckle averaging offers one unique advantage over other mitigation strategies, however, in that no changes are required to the existing footprint of the AO system. With that said, our discussion here is not limited strictly to dynamic speckle averaging. In fact, one can generalize the concept of uncorrelated speckle frames as 'degrees of freedom' afforded through any of the aforementioned techniques (or combination thereof). At the very least, dynamic speckle averaging provides a baseline method for developing more refined speckle-mitigation strategies.

In what follows, we first explain the setup used for our wave-optics simulations by parameterizing the Kolmogorov turbulence and frozen flow used in our horizontal-propagation path. We further explore this trade space by examining the impact of various beacon sizes on the speckle observed in the pupil plane. Next, we present our results from both a time-domain and steady-state perspective. Both perspectives allow us to discuss the significance of our results while establishing specifications for a nominal AO system that incorporates speckle averaging. In closing, we compare our recommendations to commercial-off-the-shelf (COTS) product availability.

[3] In so doing, we neglect the effects of uplink scintillation. Such effects are beyond the scope of the present analysis. Future studies should quantify the impacts of uplink scintillation using both compensated and uncompensated illumination to create the extended beacon.

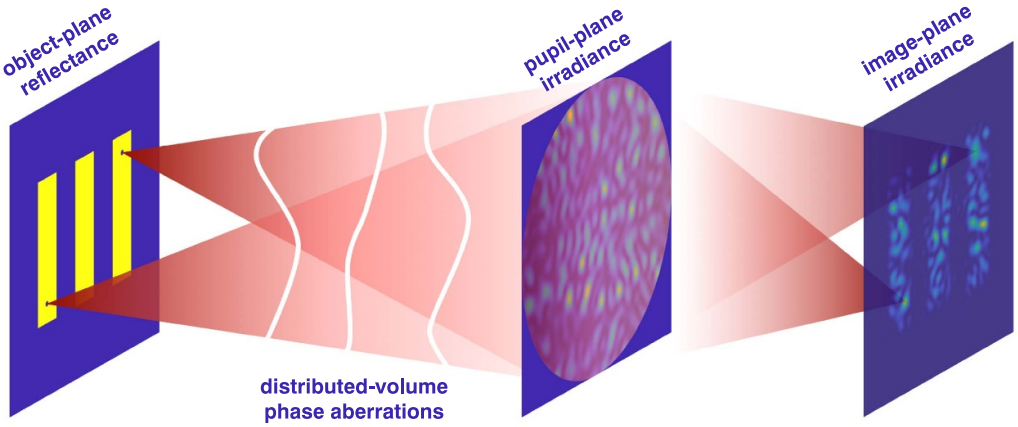

Figure 1. Illustration of how anisoplanatism results from an extended source and distributed-volume phase aberrations.

Before moving on to the next section, it is worth reiterating that the results presented in this paper demonstrate speckle averaging as an effective strategy for reducing measurement error associated with extended beacons. Even so, these performance gains steadily diminish as beacon anisoplanatism grows in its influence. This outcome serves as novel contribution to the AO research community, as a thorough trade-space exploration over horizontal propagation paths is not currently found within the peer-reviewed literature.

2. Background and theory

To set the stage for the analysis that follows, it is our intention to model extended beacons of various sizes. We do so via plane-wave illumination of square objects, such that the scattered-beacon illumination experiences both object- and atmosphere-induced phase aberrations as it propagates from the object plane to the pupil plane. These phase aberrations give rise to both speckle and scintillation, respectively, in the received irradiance.

Provided the received irradiance, we close the loop on a nominal AO system comprised of an SHWFS in the Fried geometry, a least-squares phase reconstructor, a continuous-face-sheet DM, and a leaky integrator control law [18]. Figure 2 diagrams this setup. Here, the matrices $\boldsymbol{K}$, $\boldsymbol{G}$ and $\boldsymbol{H}$ represent, respectively, the leaky-integrator controller, a continuous-face-sheet DM, and an SHWFS in the Fried geometry; the vectors $\boldsymbol{R}$, $\boldsymbol{E}$, $\boldsymbol{U}$, $\boldsymbol{D}$ and $\boldsymbol{Y}$ refer to, respectively, the reference input, the error signal, the control signal, the input disturbance (i.e. aberrated beacon) and the phase-compensated output. Note that the SHWFS and DM respectively sense and correct for the phase aberrations induced by atmospheric turbulence using the compensation offered by the integrator in this multiple-input, multiple-output control loop (hence the use of matrices). Using this setup, we compensate an outgoing laser beam and focus it from the pupil plane to the object plane along the same horizontal propagation path with Kolmogorov turbulence and frozen flow. In the object plane, we score closed-loop performance as a function of the strength of uncorrelated speckle and beacon anisoplanatism. We also investigate the framerates needed to achieve good closed-loop performance (i.e. maximize the power in the bucket).

With this setup in mind, we review in this section the theoretical inputs needed for our wave-optics simulations.

2.1. Kolmogorov turbulence

The Fried parameter (r_0) defines a circular area in the pupil plane over which the RMS phase error is approximately 1 rad [19, 20]. Because we are comparing closed-loop performance from an extended beacon against that from a point-source beacon, we assume spherical-wave propagation throughout the following analysis. Accordingly, we take the spherical-wave expression for r_0 as [21]

$$r_{0,\mathrm{sw}} = \left[0.423k^2 \int_0^{Z_1} C_n^2(z)\left(1-\frac{z}{Z_1}\right)^{5/3} \mathrm{d}z\right]^{-3/5} \xrightarrow{\text{horiz.}} \left(0.159k^2 C_n^2 Z_1\right)^{-3/5}, \tag{1}$$

where $k = 2\pi/\lambda$ is the angular wavenumber, λ is the wavelength of light, $C_n^2(z)$ is the path-dependent refractive index structure parameter, Z_1 is the propagation distance from the object plane to the pupil plane (i.e. $0 \leqslant z \leqslant Z_1$), and C_n^2 is the constant-valued refractive index structure parameter when assuming horizontal propagation paths.

In order to begin prescribing numerical values to our nominal AO system, we first take the overall pupil-plane aperture diameter D to be 30 cm (typical of modern-day beam-control systems [22]). We then assume $D/r_0 = 10$ for moderate seeing conditions without centroid anisoplanatism due to scintillation becoming a significant issue [23]. Subaperture width d should be no larger than r_0 [24], but taking d to be no smaller than r_0 maximizes flexibility in exploring larger objects under isoplanatic conditions. We can now rearrange equation (1) to

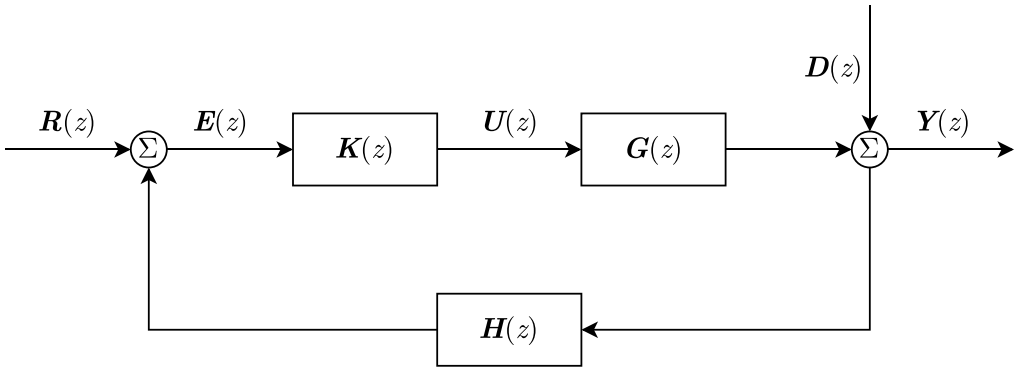

Figure 2. Block diagram of a nominal AO system operating in a null-seeking control loop using a leaky-integrator control law.

back out our constant-valued refractive-index structure parameter C_n^2 in terms of r_0 as

$$C_n^2 = \frac{0.160\lambda^2}{Z_1 r_0^{5/3}}. \tag{2}$$

Knowing C_n^2 also allows us to calculate the Rytov number, which for a spherical wave takes the form [25]

$$\begin{aligned}\mathcal{R}_{\mathrm{sw}} &= 0.563k^{7/6}\int_0^{Z_1} C_n^2(z)\left[z\left(1-\frac{z}{Z_1}\right)\right]^{5/6}\mathrm{d}z \\ &\xrightarrow{\text{horiz.}} 0.124k^{7/6}C_n^2 Z_1^{11/6}.\end{aligned} \tag{3}$$

With weak scintillation conditions (i.e. when $\mathcal{R}_{\mathrm{sw}} \lesssim 0.25$), the Rytov number estimates the log-amplitude variance (σ_χ^2) observed in the pupil plane. In other words, $\mathcal{R}$ provides a gauge for the amount of scintillation in weak Kolmogorov turbulence. This is the regime in which we choose to operate, as scintillation begins to saturate with higher Rytov numbers. In addition, branch points and cuts in the pupil-plane phase function (due to total-destructive interference) eventually sabotage our ability to perform phase compensation effectively [26–32]. The reader should note that speckle also induces branch points and cuts in the pupil-plane phase function (again, due to total-destructive interference). This outcome serves as yet another reason to perform speckle averaging to mitigate their effects.

The isoplanatic angle also plays a role in our analysis as the beacon grows in size. For all intents and purposes, θ_0 describes an angular path difference that causes a residual RMS wavefront error of approximately 1 rad (much like r_0 for the pupil-plane coherence area). We calculate θ_0 as [33]

$$\begin{aligned}\theta_0 &= \left[2.91k^2\int_0^{Z_1} C_n^2(z)\,z^{5/3}\mathrm{d}z\right]^{-3/5} \\ &\xrightarrow{\text{horiz.}} \left(1.09k^2 C_n^2 Z_1^{8/3}\right)^{-3/5}.\end{aligned} \tag{4}$$

Under the paraxial approximation, we can then multiply this angle by the propagation distance to find the total length across our isoplanatic patch in linear space as $W_0 = \theta_0 Z_1$ [34].

We also include in our analysis the temporal dynamics of Kolmogorov turbulence, specifically as it relates to sampling requirements. Assuming Taylor's frozen-flow hypothesis, the Greenwood frequency represents the 3-dB bandwidth at which a continuous-control AO system produces 1 rad of residual RMS wavefront error. We calculate the Greenwood frequency as [35]

$$\begin{aligned}f_{\mathrm{G}} &= 2.31\lambda^{-6/5}\left[\int_0^{Z_1} C_n^2(z)\,v_{\mathrm{w}}^{5/3}(z)\,\mathrm{d}z\right]^{3/5} \\ &\xrightarrow{\text{horiz.}} \left(0.102k^2 C_n^2 v_{\mathrm{w}}^{5/3} Z_1\right)^{3/5},\end{aligned} \tag{5}$$

assuming not only C_n^2 but also transverse wind speed v_{w} remains constant along a horizontal propagation path.

2.2. Digital controls

Modern control systems favor digital computers for controller implementation as they tend to be more robust, adaptable, compact, and cost effective than their analog counterparts [36]. A rule of thumb in digital control theory is that sampling at a minimum of 30× the system bandwidth (i.e. the Greenwood frequency in our case) yields adequate closed-loop performance [37]. Because a sample rate (f_{s}) of 10–20× the Greenwood frequency is also frequently cited in the literature [38], we expand our trade space to cover three distinct cases: $f_{\mathrm{s}} = 10f_{\mathrm{G}}$, $f_{\mathrm{s}} = 20f_{\mathrm{G}}$ and $f_{\mathrm{s}} = 40f_{\mathrm{G}}$.

The reader should note that the three distinct cases mentioned above represent base sample rates without taking any speckle averaging into consideration. With speckle averaging, these become 'effective' sample rates within which we count the number of averaged subframes per sample as M. For example, an effective sample rate of $f_{\mathrm{s}} = 40f_{\mathrm{G}}$ with subframe averaging of $M = 2$ would require the actual sampling frequency $Mf_{\mathrm{s}} = 80f_{\mathrm{G}}$. With this example in mind, we now determine the total number of samples (N_{s}) required to close the loop in simulation.

We assume that the servomechanism of our control loop is a first-order leaky integrator with rest initial conditions. Looking back to figure 2, the difference equation governing control block $\boldsymbol{K}$ is thus [39]

$$\boldsymbol{u}[nT] = a\boldsymbol{u}[(n-1)T] + b\boldsymbol{e}[nT], \tag{6}$$

where $\boldsymbol{u}$ is the control signal, n is a control variable for iteration, T is the sampling period, $a<1$ is the servo leakage coefficient, $b>0$ is the forward-loop gain coefficient, and $\boldsymbol{e}$ is the error signal that feeds into the controller. Aside from its straightforward implementation as a control law, this leaky integrator provides both the smoothing qualities of a low-pass filter and the stabilization benefits associated with leakage [18]. The Z transform of equation (6) yields a closed-loop transfer function of

$$\begin{aligned}\boldsymbol{K}(z) &= \frac{\boldsymbol{U}(z)}{\boldsymbol{E}(z)} \\ &= \frac{bz}{z-a}.\end{aligned} \tag{7}$$

Assuming a flattened DM, the sensitivity (a.k.a. disturbance-rejection) function is

$$\begin{aligned}\boldsymbol{S}(z) &= \frac{\boldsymbol{Y}(z)}{\boldsymbol{D}(z)} \\ &= \frac{1}{1+\boldsymbol{K}(z)} \\ &= \frac{z-a}{(1+b)z-a}\end{aligned} \tag{8}$$

with a single closed-loop pole at

$$z = \frac{a}{1+b}. \tag{9}$$

The 2% settling time is then

$$T_\mathrm{s} = \frac{\ln(0.02)\,T}{\ln[a/(1+b)]}. \tag{10}$$

To understand steady-state performance trends while minimizing simulation runtimes, we thus simulate

$$N_\mathrm{s} = \left\lceil \frac{2\ln(0.02)}{\ln[a/(1+b)]} \right\rceil \tag{11}$$

time steps on each run for twice the 2% settling time. For reference, figure 3 shows discrete-time Bode plots of equation (7) with the substitution $z = \mathrm{e}^{j2\pi fT}$. Sampling at 10, 20 and 40 times our Greenwood frequency yields 3 dB temporal bandwidths (f_bw) of 118, 236 and 472 Hz, respectively.

2.3. Beacon characteristics

We now consider the size of our extended beacon and its effect on observed speckle in the pupil plane. For this purpose, we estimate the average linear distance across a single speckle corresponding to a beacon of width W as $\lambda Z_1/W$ [40]. We then introduce the subaperture–object Fresnel number as

$$n_\mathrm{obj} = \frac{d}{\lambda Z_1/W}, \tag{12}$$

where d is again the subaperture width. Equation (12) provides us with a gauge for the average number of speckles across the width of each SHWFS subaperture [12, 13]. We can also rearrange variables to show that

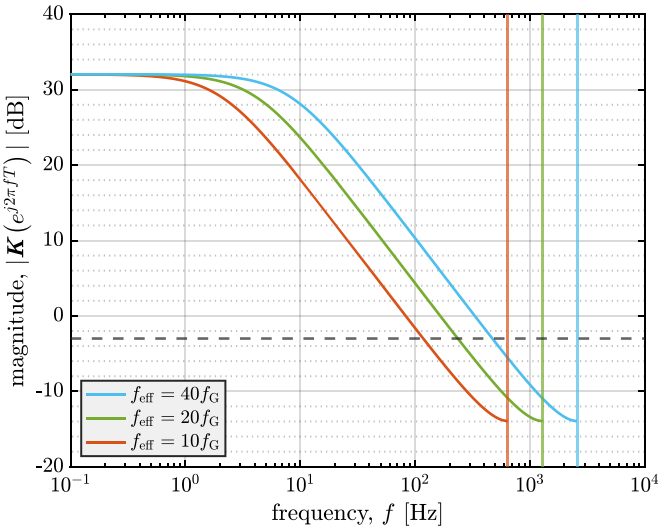

Figure 3. Bode magnitude plots of closed-loop sensitivity functions corresponding to servos implementing leaky-integrator control at various sample rates, relative to the Greenwood frequency; vertical lines indicate Nyquist frequencies at half the respective sample rates.

$$n_\mathrm{obj} = \frac{W/Z_1}{\lambda/d} \tag{13}$$

counts the rough number of diffraction-limited resolution cells across the width of the object. Together, equations (12) and (13) indicate that larger subaperture–object Fresnel numbers correspond to greater speckle severity from more well-resolved beacons.

For practical reasons in simulation, we impose different degrees of speckle decorrelation by in-plane translation of the phase underlying beacon illumination in the object plane. Specifically, we do this by solving for in-plane translation distance in the expression for an irradiance correlation coefficient. Assuming the beacon is a square plate, this irradiance correlation coefficient becomes [5]

$$\mu_I(\Delta\Omega) = \mathrm{sinc}^2\left(\frac{W\Delta\Omega}{\lambda Z_1}\right)\mathrm{tri}^2\left(\frac{\Delta\Omega}{W}\right) \tag{14}$$

where

$$\mathrm{sinc}(w) = \frac{\sin(\pi w)}{\pi w} \tag{15}$$

and

$$\mathrm{tri}(w) = \begin{cases} 1-|w| & |w|<1 \\ 0 & |w|\geqslant 1 \end{cases}. \tag{16}$$

We set equation (14) equal to 75%, 50%, 25% and 0% so that we can numerically solve for $\Delta\Omega_0$ (the initial translation distance between consecutive subframes).

2.4. Performance metrics

We now consider a performance metric that helps us to assess closed-loop performance: normalized power in the bucket (nPIB). For this purpose, we define a diffraction-limited bucket diameter as

$$D_{\mathrm{b}} = 2.44\frac{\lambda Z_1}{D} \tag{17}$$

where D is the full-aperture diameter. This quantity describes the central lobe of an Airy disk in the far field, resulting from diffraction-limited propagation of a focused flat-top beam at range $z = Z_1$. A 'bucket' of this diameter encircles 83.8% of the initial beam power leaving the pupil plane under diffraction-limited conditions [41]. The nPIB is then a normalization of phase-compensated, turbulence-limited power by the diffraction-limited power measured in this bucket [18]:

$$\mathrm{nPIB} = \frac{\int_0^{2\pi}\int_0^{D_b/2} E_{\mathrm{tl}}(\Omega,\theta)\,\Omega\,\mathrm{d}\Omega\,\mathrm{d}\theta}{\int_0^{2\pi}\int_0^{D_b/2} E_{\mathrm{dl}}(\Omega,\theta)\,\Omega\,\mathrm{d}\Omega\,\mathrm{d}\theta}. \tag{18}$$

Here, E_{tl} and E_{dl} are the turbulence- and diffraction-limited irradiance values, respectively.

Because the position of our diffraction-limited bucket is fixed in the object plane, nPIB is sensitive to residual tilt in the outgoing beam and is analogous to an on-axis Strehl ratio. To provide a baseline for comparison of simulation results against theory, we can use the extended Maréchal approximation to calculate an expected on-axis Strehl ratio as [42]

$$\langle S\rangle = \exp\left(-\sigma_{\mathrm{tot}}^2\right). \tag{19}$$

Here, σ_{tot}^2 is the total variance associated with wavefront error which goes as [38]

$$\sigma_{\mathrm{tot}}^2 = \sigma_{\mathrm{fit}}^2 + \sigma_{\chi}^2 + \sigma_{\mathrm{tmp}}^2 + \sigma_{\mathrm{iso}}^2 \tag{20}$$

assuming we can safely neglect sensor noise[4]. The first term of equation (20) is spatial fitting error, which we have from Noll as [19]

$$\sigma_{\mathrm{fit}}^2 = 0.294\,(D/r_0)^{5/3} N_{\mathrm{act}}^{-\sqrt{3}/2} \tag{21}$$

with N_{act} being the number of active actuators behind the DM. The second term of equation (20) is simply the log-amplitude variance from Kolmogorov turbulence theory [43]. The third term of equation (20) describes temporal lag, which we calculate from the Greenwood frequency as [35]

$$\sigma_{\mathrm{tmp}}^2 = (f_{\mathrm{G}}/f_{\mathrm{bw}})^{5/3}, \tag{22}$$

where f_{bw} is again the 3-dB temporal bandwidth. The fourth and final term of equation (20) refers to isoplanatic error, which Fried first derived as [33]

$$\sigma_{\mathrm{iso}}^2 = (\theta/\theta_0)^{5/3}. \tag{23}$$

It is important to keep in mind that the quadrature sum in equation (20) assumes mutual independence of all noise sources involved. If surface-based aberrations were truly uncorrelated from atmospheric aberrations, we could in theory add a fifth term characterizing speckle-noise variance as [3]

$$\sigma_{\mathrm{sp}}^2 = \left[2\pi\, C\left(3.54 + \frac{2.11}{n_{\mathrm{obj}}}\right)^{-1}\right]^2. \tag{24}$$

However, it is well known that noise from speckle and scintillation couples in ways that we do not yet fully understand [44]. Furthermore, there is good reason to believe that errors arising from speckle and anisoplanatism cannot be treated independently from one another as the beacon grows in size. For these reasons, we rely on equation (20) to predict point-source performance only and investigate further degradation due to extended beacons through wave-optics simulations.

3. Modeling and simulation

In setting up our wave-optics simulations, we used the split-step beam propagation method to simulate propagation of complex optical fields along horizontal paths through the atmosphere. To model the distributed-volume phase aberrations, we used 40 independent realizations of six equally spaced Kolmogorov phase screens with frozen flow. Thus, in the results that follow we report the associated Monte Carlo averages.

To create extended beacons of various sizes, we simulated on-axis, plane-wave illumination of square objects. For this purpose, we defined our object length W by the subaperture–object Fresnel number from equation (12). We then tested six different values of n_{obj} in increasing powers of two. As a visual aid, figure 4 highlights the inverse relationship between object size and the total number of received speckles. The object sizes that correspond to these values are roughly equidistant from our fixed isoplanatic patch size W_0 on either side of the inequality. As we will see in the results that follow, the interplay between W and W_0 gives us a gauge for when beacon anisoplanatism becomes a performance-limiting factor.

As shown in figures 4(a) and (c), we assumed that the rough-surface statistics were delta-correlated over the extent of our square objects. To satisfy this assumption, we defined the phase at each object mesh point as a uniformly distributed random draw on the interval $[-\pi, \pi)$. For each simulated time

[4] The wave-optics simulations presented in this paper do not include the effects of detection noise. Such effects are beyond the scope of the present analysis. Future studies should quantify the impacts of detection noise when using fast-framing FPAs.

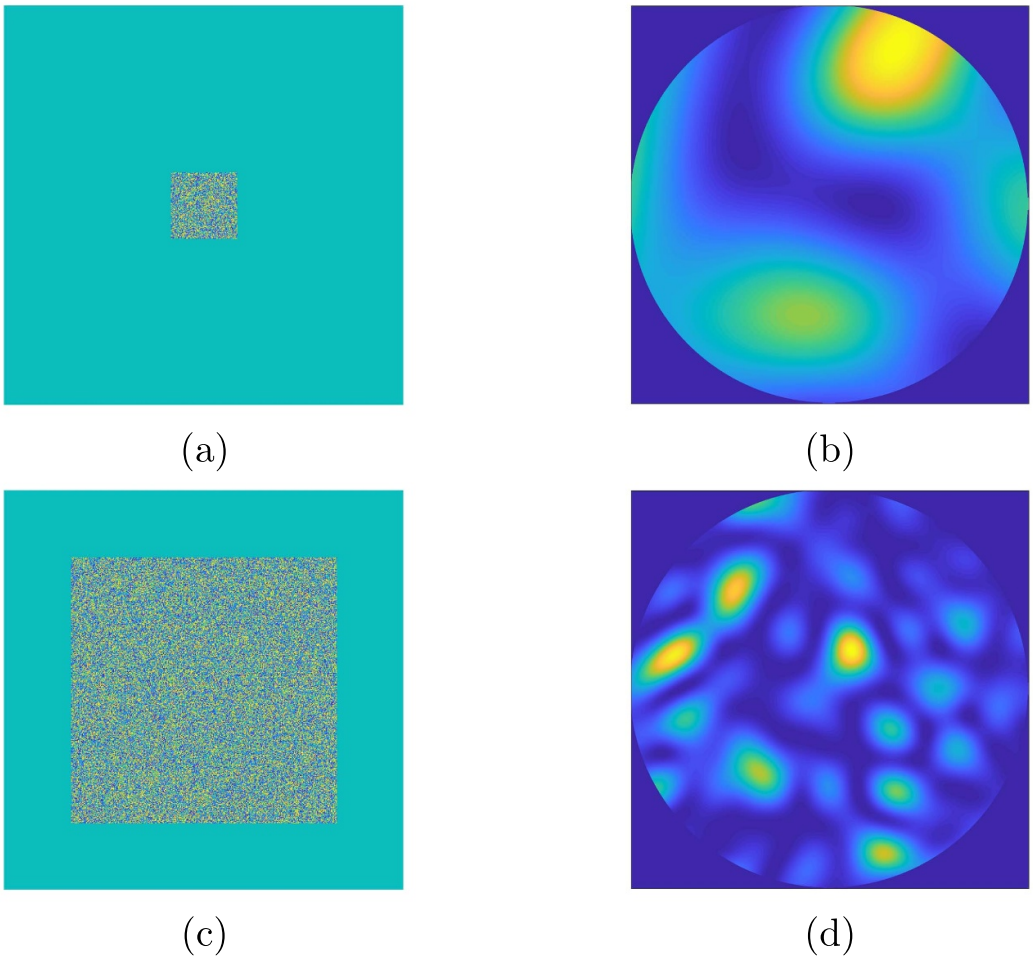

Figure 4. Visual aid to show that as the object size increases from (a) to (c), the total number of received speckles increases from (b) to (d).

step, we then solved equation (14) for the incremental translation distance $\Delta\Omega_0$ of underlying phase that decorrelated pupil-plane speckle by 25%, 50%, 75% or 100%. We achieved partial decorrelation of speckle without repetition by following the procedure outlined in reference [4]. Alternatively, we reseeded the random phase drawn in the object plane for fully uncorrelated frame-to-frame speckle.

To prevent numerical artifacts such as aliasing due to the periodic nature of discrete Fourier transforms involved in propagation, we defined our sampling parameters such that Nyquist sampling [45], critical sampling [46], and speckle sampling [47] constraints were all satisfied. We also spatially filtered the simulated rough-surface objects to remove high divergence angles outside of the entrance-pupil collection area [48]. We used the WavePlex Toolbox for MATLAB® from Prime Plexus[5] to simulate rough-surface scattering, propagation through turbulence, tilt measurement with a centroid tracker, first-order tilt correction with a fast-steering mirror, wavefront sensing with an SHWFS in the Fried geometry, least-squares phase reconstruction with a leaky integrator control law, and phase compensation using a continuous-face-sheet DM.

Given the vast number of simulation inputs available within our modeling tradespace, an exhaustive matrix test of all possible combinations is neither practical nor would such an undertaking be digestible to the reader. For this reason, we provided different perspectives by defining two different parameterizations of the general simulation routines described. The first prioritizes study of partial speckle decorrelation according to equation (14) under isoplanatic conditions. One of the main implications of this approach is that we sacrifice sampling resolution in the pupil plane ($d/r_0 = 1$) in exchange for beacon isoplanatism, which means limited peak performance even in the case of a point-source beacon due to fitting error. The second parameterization therefore emphasizes better peak performance by improving spatial resolution ($d/r_0 = 0.5$) at the expense of beacon isoplanatism, limiting the beacon

[5] T J Brennan is the sole author of the WavePlex Toolbox for MATLAB® with correspondence to the following address: Prime Plexus, 650 N Rose Drive #439, Placentia, CA 92 870, USA.

Table 1. Physical and numerical parameters used in wave-optics simulations of closed-loop AO with partially correlated speckle.

	Parameter	Value(s)
physical	Optical wavelength, λ (μm)	1
	Propagation distance, Z_1 (m)	283
	Aperture diameter, D (cm)	30
	Subaperture width, d (cm)	3
	Subaperture–object Fresnel number, n_{obj}	$\left\{1/8, 1/4, 1/2, 1, 2, 4, 8\right\}$
	Lenslet Fresnel number, n_{lod}	8
	Lenslet focal length, $f = Z_2$ (m)	113
	Total actuator count, N_{act}	101
	Refractive-index structure constant, C_n^2 ($\text{m}^{-2/3}$)	1.96×10^{-13}
	Spherical-wave Rytov number, $\mathcal{R}_{\text{sw}}$	0.0658
	Spherical-wave Fried parameter, r_0 (cm)	3
	Isoplanatic angle, θ_0 (μrad)	33.3
	Piston-removed isoplanatic angle, θ_1 (μrad)	40.9
	Piston/tip/tilt-removed isoplanatic angle, θ_3 (μrad)	43.9
	Greenwood frequency, f_{G} (Hz)	129
	Effective sample rate, f_{s} (kHz)	$\{1.29, 2.57, 5.14\}$
	Servo leakage coefficient, a	0.99
	Servo gain coefficient, b	0.40
numerical	Grid points per side, $N \times N$	2048×2048
	Object-plane grid spacing, δ_{obj} (μm)	259
	Pupil-plane grid spacing, δ_{pup} (μm)	534
	Image-plane grid spacing, δ_{img} (μm)	103
	Object-plane side length, S_{obj} (mm)	529
	Pupil-plane side length, S_{pup} (m)	1.09
	Image-plane side length, S_{img} (mm)	211

sizes that we can expect to allow for speckle averaging under isoplanatic conditions. We also restrict our attention to fully uncorrelated speckle in this second parameterization. The numerical values associated with these parameterizations are summarized in tables 1 and 2, respectively.

4. Results and discussion

In this section, we first present a selection of closed-loop results for both time-domain and steady-state performance with partially correlated frame-to-frame speckle. We then present a selection of closed-loop results for both time-domain and steady-state performance with relaxed isoplanatic constraints and fully uncorrelated frame-to-frame speckle. In all cases, we also provide both point-source and uncompensated results for reference. Provided these results, we also discuss the impacts of beacon anisoplanatism and sampling rates.

4.1. Partially correlated speckle

Figure 5 displays selected nPIB results in the time domain with $f_{\text{s}} = 40 f_{\text{G}}$. Specifically, figure 5(a) shows the case of no speckle averaging, whereas figures 5(b) and (c) show the case of 32 subframes averaged per frame with 25% and 100% decorrelation, respectively, between consecutive subframes. We show only the 25% and 100% decorrelation cases because the 50%, and 75% decorrelation cases yielded similar results. In general, larger extended beacons give rise to poorer closed-loop performance in terms of final nPIB value. Speckle averaging mitigates this performance degradation to some extent, with the smallest extended beacons and degrees of correlation enabling the greatest performance buyback. In these best-case scenarios, extended beacons closely approach point-source performance. The diminishing returns of speckle averaging are readily apparent as the extended beacon size outgrows the isoplanatic patch size in the neighborhood of $n_{\text{obj}} \approx 1$, especially when comparing the 25% decorrelation case to the 100% decorrelation case. Note that the anisoplanatic regime appears to occur somewhat past the expected isoplanatic patch size where $n_{\text{obj}} \approx 1$ and may actually correspond more closely to the piston- or piston/tip/tilt-removed 'extended' isoplanatic angle [49] (cf tables 1 and 2).

Figure 6 displays selected nPIB results in steady state with $f_{\text{s}} = 40 f_{\text{G}}$. Specifically, figure 6(a) shows results as a function of partially correlated speckle averaging at 25% decorrelation between consecutive subframes, whereas figure 6(b) shows results for 100% decorrelation. Again, we only show the 25% and 100% decorrelation case because the 50% and 75% decorrelation cases yielded similar results. Analogous to figure 5, we see that smaller beacons begin to approximate point-source performance. We also see that the temporal noise present in figure 5 produces some fluctuations in the steady-state trends

Table 2. Physical and numerical parameters used in wave-optics simulations of closed-loop AO with fully uncorrelated speckle.

	Parameter	Value(s)
physical	Optical wavelength, λ (μm)	1
	Propagation distance, Z_1 (km)	1
	Aperture diameter, D (cm)	30
	Subaperture width, d (cm)	1.5
	Subaperture–object Fresnel number, n_{obj}	$\left\{1/20, 1/10, 1/5, 2/5, 4/5, 8/5\right\}$
	Lenslet Fresnel number, n_{lod}	4.4
	Lenslet focal length, $f = Z_2$ (m)	51.1
	Total actuator count, N_{act}	357
	Refractive-index structure constant, C_n^2 ($\mathrm{m}^{-2/3}$)	5.53×10^{-14}
	Spherical-wave Rytov number, $\mathcal{R}_{\mathrm{sw}}$	0.189
	Spherical-wave Fried parameter, r_0 (cm)	3
	Isoplanatic angle, θ_0 (μrad)	9.42
	Piston-removed isoplanatic angle, θ_1 (μrad)	11.6
	Piston/tip/tilt-removed isoplanatic angle, θ_3 (μrad)	12.4
	Greenwood frequency, f_{G} (Hz)	129
	Effective sample rate, f_{s} (kHz)	$\{1.29, 2.57, 5.14\}$
	Servo leakage coefficient, a	0.99
	servo gain coefficient, b	0.40
numerical	Grid points per side, $N \times N$	512×512
	Object-plane grid spacing, δ_{obj} (mm)	1.40
	Pupil-plane grid spacing, δ_{pup} (mm)	1.40
	Image-plane grid spacing, δ_{img} (μm)	71.4
	Object-plane side length, S_{obj} (cm)	71.6
	Pupil-plane side length, S_{pup} (cm)	71.6
	image-plane side length, S_{img} (mm)	36.6

that would be alleviated through further time and/or ensemble averaging.

To help summarize the partially correlated trade space, figure 7 shows results as a function of the subaperture-object Fresnel number n_{obj} with 4-subframe averaging, which serves as the 'knee in the curve' for the results presented in figure 6. As n_{obj} increases, so do the effects of beacon anisoplantism. In fact, these effects become the most limiting across the entire partially correlated trade space.

In figure 7, we find that equation (19) together with equation (20) accurately predicts point-source performance within a reasonable error margin at ∼0.650.

4.2. *Fully uncorrelated speckle*

Figure 8 displays selected nPIB results in the time domain with $f_{\mathrm{s}} = 40 f_{\mathrm{G}}$ and fully uncorrelated speckle. Specifically, figure 8(a) corresponds to the one-frame case, whereas figure 8(b) corresponds to averaging four mutually uncorrelated subframes within a single frame. We show only the one- and four-frame cases because the two-, eight-, 16-, and 32-frame cases yielded similar results. Rather than simulating only the number of time steps necessary to double the 2% settling time, these cases simulate twice the time it takes for transverse wind to 'clear' the aperture twice according to Taylor's frozen-flow hypothesis:

$$T_{\mathrm{c}} = \frac{D}{v_{\mathrm{w}}} f_{\mathrm{s}}, \tag{25}$$

such that

$$N_{\mathrm{s}} = \left\lceil \frac{2D}{v_{\mathrm{w}}} f_{\mathrm{s}} \right\rceil. \tag{26}$$

We see now that the improved fitting parameters from table 2 have afforded better approximation of point-source performance with smaller beacons as compared with figure 5.

Figure 9 displays selected nPIB results in steady state with f_{s} from $10 f_{\mathrm{G}}$ to $40 f_{\mathrm{G}}$ as a function of fully uncorrelated speckle averaging. Specifically, figures 9(a) and (b) correspond to subaperture–object Fresnel numbers of $1/20$, $1/10$, $1/5$, $2/5$, $4/5$ and $8/5$, respectively. As predicted, we see better smoothing here than in figure 6 as a result of the increase in simulated runtimes allowing for more time averaging beyond settling times. Note that in figure 9(a) speckle averaging actually reduces the steady-state nPIB with insufficient temporal sampling at $10 f_{\mathrm{G}}$; this is because of outdated atmospheric data compounding in the temporal equivalent of spatial path averaging.

To help summarize the fully uncorrelated trade space, figure 10 shows results as a function of the subaperture-object Fresnel number n_{obj} with 4-subframe averaging, which serves as the 'knee in the curve' for the results presented in figure 9. Similar to figure 7, as n_{obj} increases, so do the effects of beacon

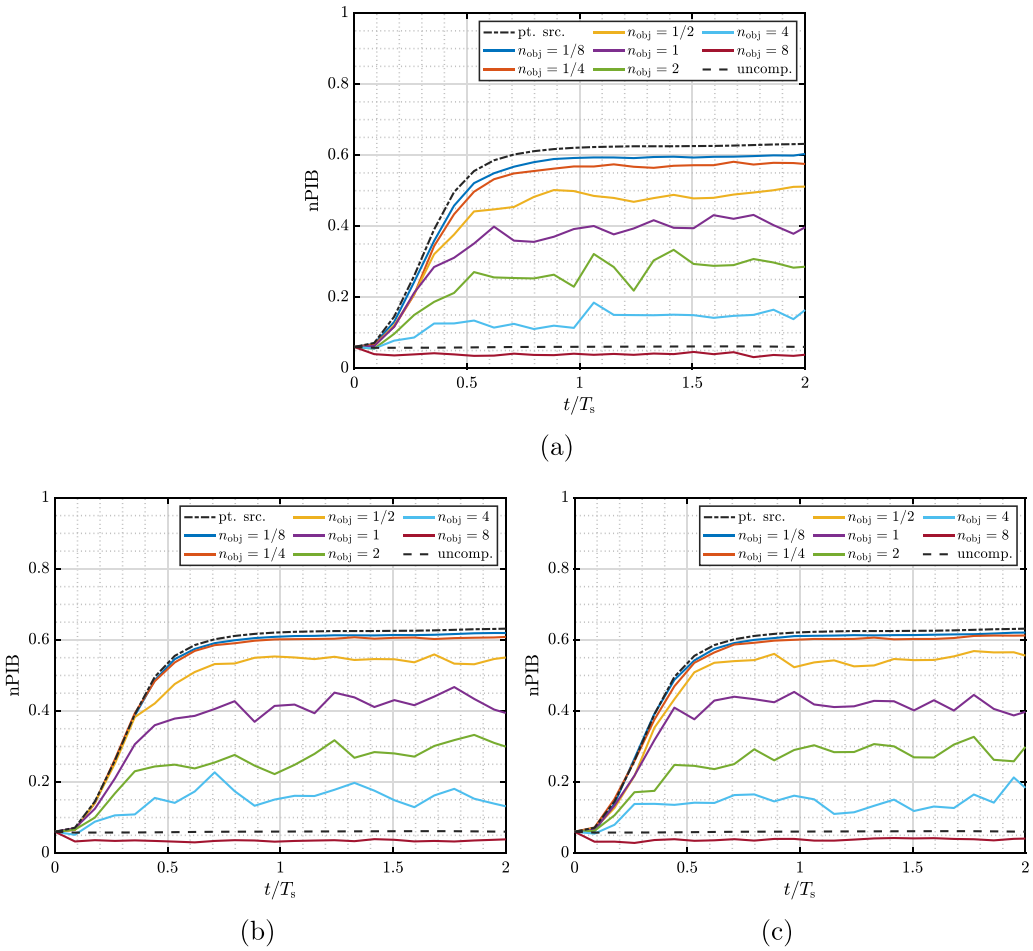

Figure 5. Time-domain nPIB results with $f_s = 40f_G$ and (a) no speckle averaging, as well as 32-subframe averaging at (b) 25% and (c) 100% decorrelation of speckle between consecutive subframes.

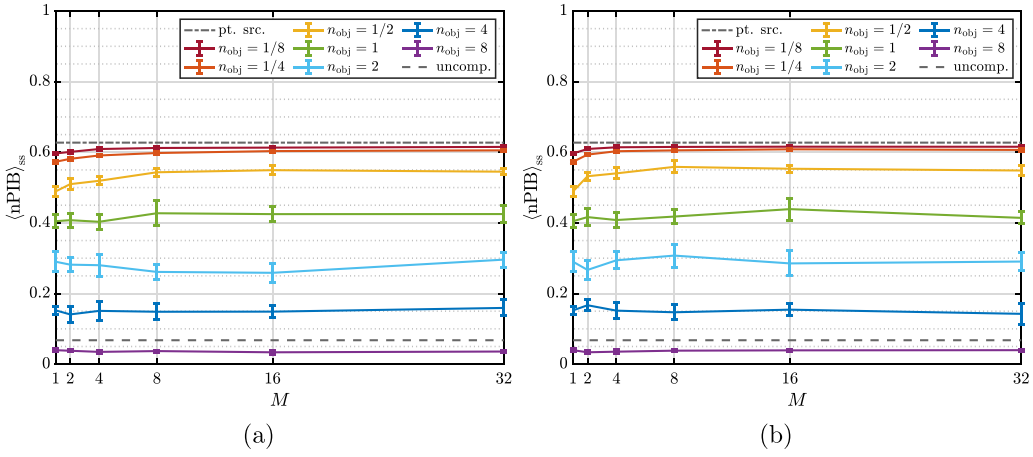

Figure 6. Steady-state nPIB results as a function of M-subframe averaging with $f_s = 40f_G$ at (a) 25% and (b) 100% decorrelation of speckle between consecutive subframes.

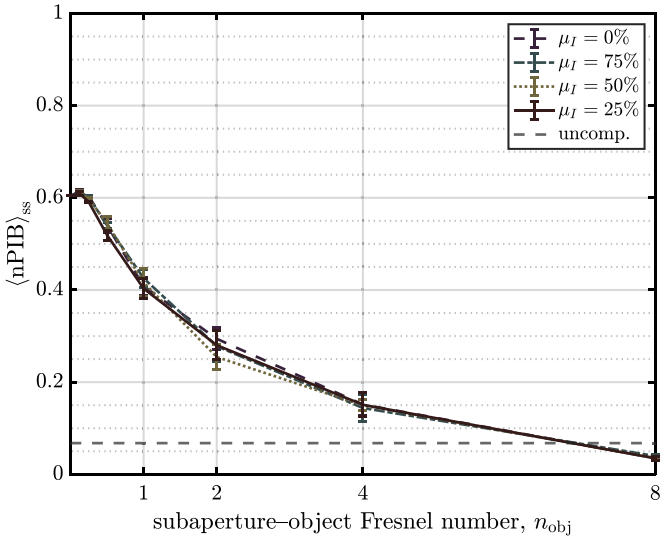

Figure 7. Steady-state nPIB results as a function of subaperture-object Fresnel number with partially correlated speckle, $f_{\mathrm{s}} = 40 f_{\mathrm{G}}$, and 4-subframe averaging.

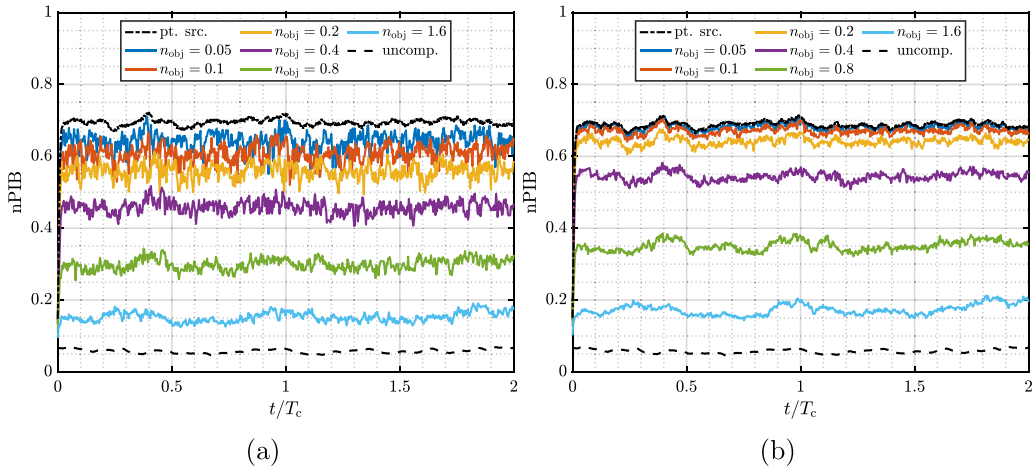

Figure 8. Time-domain nPIB results with $f_{\mathrm{s}} = 40 f_{\mathrm{G}}$ and (a) no speckle averaging, as well as (b) four-subframe averaging for fully uncorrelated speckle between consecutive subframes.

anisoplanatism. In fact, these effects become the most limiting across the entire uncorrelated trade space.

In figure 10, we again find that equation (19) together with equation (20) accurately predicts point-source performance within a reasonable error margin at ∼0.679 for the highest temporal sampling of $f_{\mathrm{s}} = 40 f_{\mathrm{G}}$, but it underpredicts performance at ∼0.529 and ∼0.240 for $f_{\mathrm{s}} = 20 f_{\mathrm{G}}$ and $f_{\mathrm{s}} = 10 f_{\mathrm{G}}$, respectively.

4.3. Bandwidth considerations

Anisoplanatic limitations aside, we point out somewhat trivially that increasing the effective sample rate and number of speckle averages, in addition to decreasing the object Fresnel number, generally produces the best closed-loop results. However, sampling at even 20 times the Greenwood frequency f_{G} may not be realizable with commercial-off-the-shelf availability in mind if $f_{\mathrm{G}} = 129$ Hz. In what follows, we will analyze this last point with the parameters used in our wave-optics simulations (cf tables 1 and 2).

Provided a minimum 8 pixels across each subaperture and 20 total subapertures across the full aperture, we require a linear FPA resolution of $8 \times 20 = 160$ from our SHWFS design. Current hardware limitations throttle the framerates of fast-framing FPAs (with responsivity at $\lambda = 1$ μm) to ∼20 kfps for a region of interest (ROI) with dimensions 160×160 pixels [50]. If we consider our most aggressive effective sample rate of $f_{\mathrm{s}} = 40 f_{\mathrm{G}}$ and the knees in the curves of figures 6 and 9 at $M \approx 4$, we require an actual sampling frequency (framerate) of $M f_{\mathrm{s}} = 160 f_{\mathrm{G}} \approx 20.6$ kHz. Thus, our most aggressive speckle-averaging goal is for the most part realizable with respect to commercial-off-the-shelf hardware if $f_{\mathrm{G}} = 129$ Hz.

These comments assume that the Greenwood frequency f_{G} remains constant in time. In any case, we have determined empirically that the loop closes consistently when our 3 dB

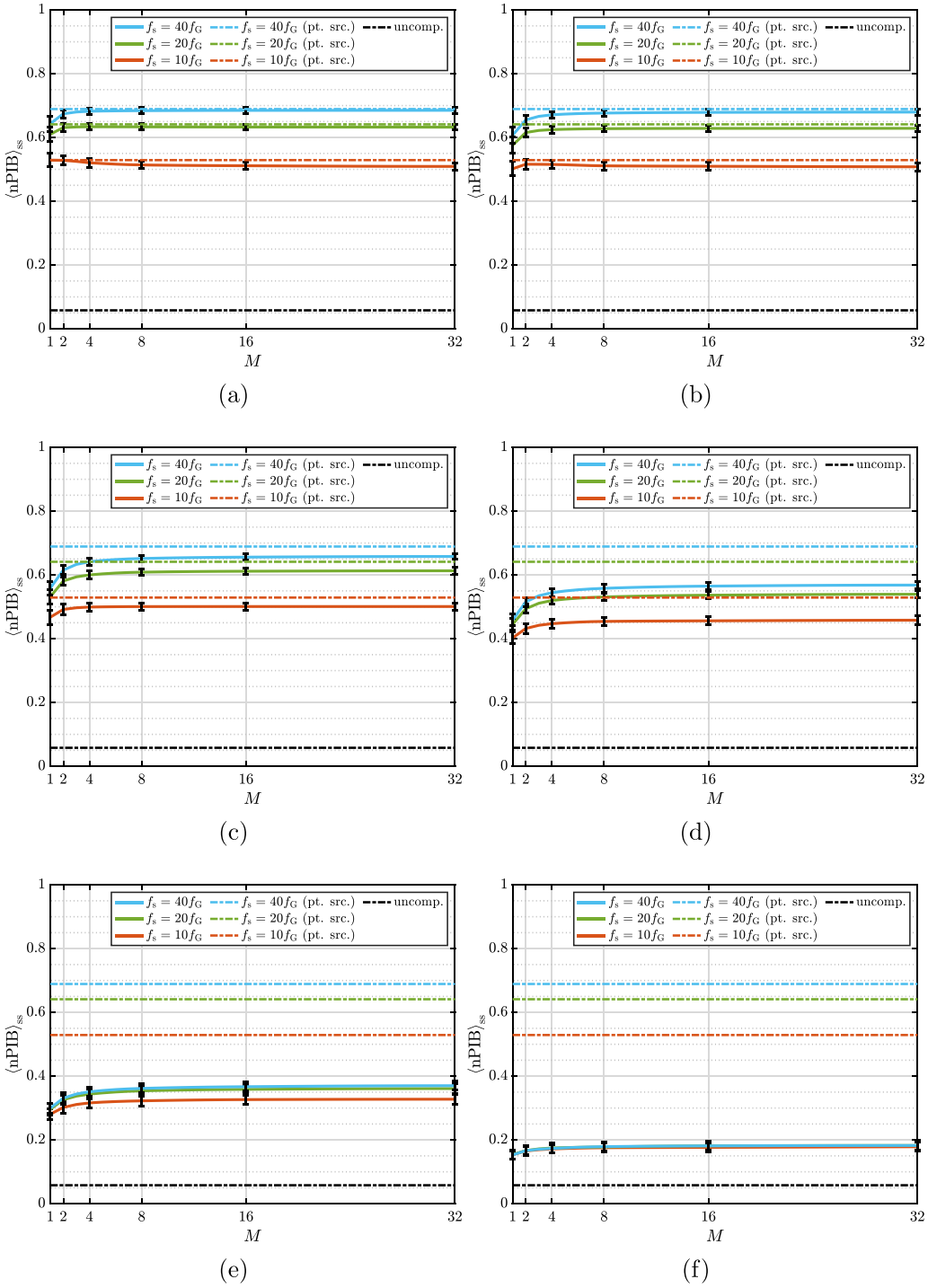

Figure 9. Steady-state nPIB results comparing $f_s = 40f_G$, $20f_G$ and $10f_G$ for various degrees of speckle averaging with fully uncorrelated speckle between consecutive subframes at (a) $n_{obj} = 1/20$, (b) $n_{obj} = 1/10$, (c) $n_{obj} = 1/5$, (d) $n_{obj} = 2/5$, (e) $n_{obj} = 4/5$ and (f) $n_{obj} = 8/5$.

bandwidth is at least approximately $1.5f_G$. If $f_G = 129$ Hz, then $1.5f_G \approx 194$ Hz. Through Bode analysis, this empirically determined rule of thumb implies an actual framerate of only 5.14 kHz $\ll$ 20 kfps, leaving plenty of headroom with respect to closed-loop stability.

With the above results and observations in mind, the overall lessons learned in these studies are as follows:

(i) The presence of speckle noise harms closed-loop AO performance, with the worst cases corresponding to larger extended beacons.

(ii) Speckle averaging can buy back performance under isoplanatic conditions, with the best cases corresponding to minimal speckle correlation between averaged subframes.

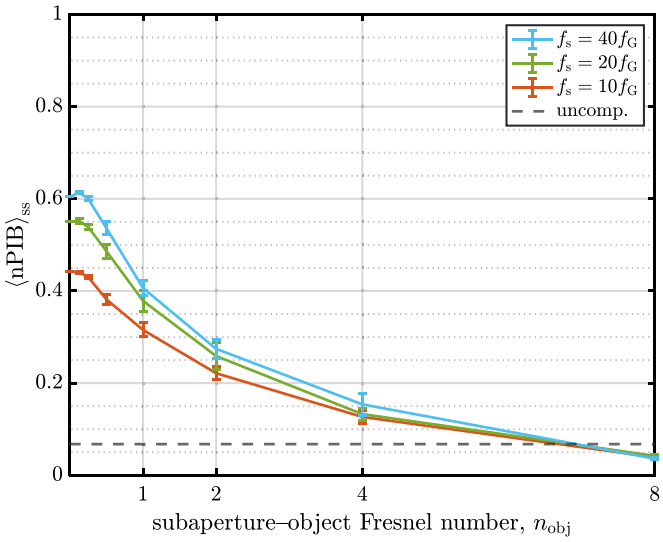

Figure 10. Steady-state nPIB results as a function of subaperture-object Fresnel number with fully uncorrelated speckle, varying sample rates, and 4-subframe averaging.

(iii) Path averaging due to beacon anisoplanatism precludes any performance gains through speckle averaging once the extended beacon size exceeds the isoplanatic patch size.
(iv) Point-source performance dictates potential for performance buyback through speckle averaging, in our cases ranging from ∼9% relative performance boost (∼5% absolute) with $d/r_0 = 1$ to ∼17% relative performance boost (∼10% absolute) with $d/r_0 = 0.5$.
(v) Inadequate temporal sampling not only impacts closed-loop performance in the absence of speckle, but can actually cause speckle averaging to impair performance even further with speckle averaging versus without.

5. Conclusion

In this paper, we investigated the use of an extended beacon with a nominal AO system. An extended beacon, in general, manifests due to the scattering of coherent illumination off of an optically rough surface and results in two phenomena: (1) speckle, which adds noise to the phase measurement, and (2) anisoplanatism, which causes multiple point-spread functions to arise within the field of view of the AO system. Together, these phenomena remain relatively unexplored in the peer-reviewed literature, as AO research typically relies on the use of a point-source beacon for optimal performance. A point-source beacon, in practice, does not give rise to speckle or anisoplanatism but is unrealistic for non-cooperative directed-energy applications. As such, in this paper we created extended beacons of various sizes using the plane-wave illumination of square targets. We then assumed that the resultant speckle was uncorrelated from one frame to the next and that there was the potential for beacon anisoplanatism. These assumptions allowed us to explore the trade space using straightforward wave-optics simulations.

Provided these wave-optics simulations, we modeled a horizontal-propagation path with Kolmogorov turbulence and frozen flow. We also modeled a nominal AO system comprised of an SHWFS in the Fried geometry, a least-squares phase reconstructor, a continuous-face-sheet DM, and a leaky integrator control law. Our approach characterized the severity of the uncorrelated speckle and beacon anisoplanatism using the object Fresnel number and the size of the target relative to the size of the isoplanatic patch, respectively.

Overall, the closed-loop results showed that speckle averaging can be an effective strategy for mitigating the noise induced by uncorrelated speckle. However, as the extended beacon grows in size, beacon anisoplanatism seems to become the limiting factor with respect to performance and negates the benefits of speckle averaging. Armed with this knowledge, future efforts should focus on increasing the effective sample rates and the number of speckle averages, in addition to decreasing the object Fresnel numbers associated with their AO systems to produce the best closed-loop results.

Data availability statement

The data cannot be made publicly available upon publication due to legal restrictions preventing unrestricted public distribution. The data that support the findings of this study are available upon reasonable request from the authors.

Acknowledgment

This material is based upon high-performance computing (HPC) resources supported by the University of Arizona's Technology and Research Initiative Fund (TRIF), University Information Technology Services (UITS), and Office for Research, Innovation, and Impact (RII) and maintained by the Research Technologies Department of UITS. Approved for public release; distribution is unlimited. M F Spencer would like to acknowledge the long-term support of the Joint Directed Energy Transition Office in completing this research. Public Affairs release approval #AFRL-2024-3941. The views expressed are those of the authors and do not necessarily reflect the official policy or position of the Department of the Air Force, the Department of Defense, or the U. S. government.

ORCID iDs

Derek J Burrell https://orcid.org/0000-0002-5647-4999
Mark F Spencer https://orcid.org/0000-0002-3803-3938

References

[1] Ageorges N and Dainty C 1997 *Laser Guide Star Adaptive Optics for Astronomy* (Kluwer Academic)
[2] Burrell D J, Follansbee J H, Spencer M F and Driggers R G 2023 *Opt. Express* **31** 38625–39
[3] Burrell D J, Spencer M F, Beason M K and Driggers R G 2023 *J. Opt. Soc. Am.* A **40** 904–13

[4] Burrell D J, Spencer M F and Driggers R G 2024 *Opt. Commun.* **572** 130960
[5] Burrell D J, Spencer M F, Zandt N R V and Driggers R G 2021 *Appl. Opt.* **60** G64–G76
[6] Burrell D J, Spencer M F, Zandt N R V and Driggers R G 2021 *Appl. Opt.* **60** G77–G90
[7] Van Zandt N R, McCrae J E and Fiorino S T 2016 *Opt. Eng.* **55** 024106
[8] Goodman J W 2020 *Speckle Phenomena in Optics: Theory and Applications* 2nd edn (SPIE)
[9] Raynor R A, Spencer M F and Moore T D 2017 Modeling coherence propagation in a homogenizing light pipe for speckle mitigation *Unconventional and Indirect Imaging, Image Reconstruction and Wavefront Sensing* vol 10410, ed J J Dolne and R P Millane (SPIE) p 104100X
[10] Hyde I V M W Basu S, Voelz D G and Xiao X 2015 *J. Appl. Phys.* **118** 093102
[11] Hyde I V M W and Spencer M F 2018 *Appl. Opt.* **57** 6403–9
[12] Van Z N R, Mc Crae J E, Spencer M F, Steinbock M J, Hyde I V M W and Fiorino S T 2018 *Appl. Opt.* **57** 4090–102
[13] Van Z N R, Spencer M F, Steinbock M J, Anderson B M, Hyde I V M W and Fiorino S T 2018 *Appl. Opt.* **57** 4103–10
[14] Noah R, Van Z, Spencer M F, McCrae J E and Fiorino S T 2018 Polychromatic speckle mitigation at surface discontinuities *IEEE Aerospace Conf.* pp 1–9
[15] Zandt N R V, Spencer M F and Fiorino S T 2019 *Appl. Opt.* **58** 2300–10
[16] Zandt N R V and Spencer M F 2020 *Appl. Opt.* **59** 1071–81
[17] Wolf E 2007 *Introduction to the Theory of Coherence and Polarization of Light* (Cambridge University Press)
[18] Merritt P and Spencer M 2018 *Beam Control for Laser Systems* 2nd edn (Directed Energy Professional Society)
[19] Noll R J 1976 *J. Opt. Soc. Am.* **66** 207–11
[20] Hickson P 2014 *Astron. Astrophys. Rev.* **22** 76
[21] Fried D L 1966 *J. Opt. Soc. Am.* **56** 1372–9
[22] Schneider J W 2007 Defense science board task force on directed energy weapons *Technical Report* Office of the Under Secretary of Defense for Acquisition, Technology and Logistics Washington
[23] Yura H T and Tavis M T 1985 *J. Opt. Soc. Am.* A **2** 765–73
[24] Tyson R K 2000 Introduction to adaptive optics *Tutorial Texts in Optical Engineering* vol T41 (SPIE)
[25] Tatarski V I 1961 *Wave Propagation in a Turbulent Medium* (McGraw-Hill)
[26] Fried D L 1998 *J. Opt. Soc. Am.* A **15** 2759–68
[27] Tyler G A 2000 *J. Opt. Soc. Am.* A **17** 1828–39
[28] Fried D L 2001 *Opt. Commun.* **200** 43–72
[29] Barchers J D, Fried D L and Link D J 2002 *Appl. Opt.* **41** 1012–21
[30] Steinbock M J, Hyde M W and Schmidt J D 2014 *Appl. Opt.* **53** 3821–31
[31] Banet M T and Spencer M F 2020 *Opt. Express* **28** 36902–14
[32] Spencer M F and Brennan T J 2022 *Opt. Express* **30** 33739–55
[33] Fried D L 1982 *J. Opt. Soc. Am.* **72** 52–61
[34] Carrano C J 2003 Anisoplanatic performance of horizontal-path speckle imaging *Advanced Wavefront Control: Methods, Devices and Applications* vol 5162, ed J D Gonglewski, M A Vorontsov and M T Gruneisen (SPIE) pp 14–27
[35] Greenwood D P 1977 *J. Opt. Soc. Am.* **67** 390–3
[36] Leigh J R 1992 *Applied Digital Control: Theory, Design and Implementation* 2nd edn (Prentice Hall International)
[37] Franklin G F, Powell J D and Workman M L 1997 *Digital Control of Dynamic Systems* 3rd edn (Addison-Wesley Longman)
[38] Tyson R K and Frazier B W 2012 *Field Guide to Adaptive Optics* 2nd edn (SPIE)
[39] Proakis J G and Manolakis D G 2021 *Digital Signal Processing: Principles, Algorithms and Applications* 5th edn (Pearson)
[40] Dainty J C 1975 Laser speckle and related phenomena *Topics in Applied Physics* (Springer)
[41] Born M and Wolf E 2019 *Principles of Optics: Electromagnetic Theory of Propagation, Interference and Diffraction of Light* 60th Anniversary (Cambridge University Press)
[42] Ross T S 2009 *Appl. Opt.* **48** 1812–8
[43] Yura H T and Fried D L 1999 Variance of the strehl ratio of an adaptive optics system *Technical Report* (The Aerospace Corporation El Segundo) p SMC-TR-99-10
[44] Holmes J F, Lee M H and Kerr J R 1980 *J. Opt. Soc. Am.* **70** 355–60
[45] Schmidt J D 2010 *Numerical Simulation of Optical Wave Propagation With Examples in Matlab®* (SPIE) p M199
[46] Voelz D 2011 *Computational Fourier Optics: A MATLAB® Tutorial* (*Tutorial Texts in Optical Engineering*) vol T89 (SPIE)
[47] Burrell D, Beck J, Beason M and Berry B 2021 Wave-optics sampling constraints in the presence of speckle and anisoplanatism *Proc. SPIE* **11836** 1183603
[48] Brennan T J, Roberts P H and Mann D C 2010 WaveProp: A wave optics simulation system for use with MATLAB® (user's guide)
[49] Burrell D, Kemnetz M, Beck J and Beason M 2022 *Efficiently Calculating Extended Isoplanatic Angles Over Horizontal Paths* (*Propagation Through and Characterization of Atmospheric and Oceanic Phenomena*) p W4F.6
[50] Neys J, Bentell J, O'Grady M, Vermeiren J, Colin T, Hooylaerts P and Grietens B 2008 *Cheetah: A High Frame Rate, High Resolution Swir Image Camera Sensors, Systems and Next-Generation Satellites XII* vol 7106, ed R Meynart, S P Neeck, H Shimoda and S Habib (SPIE) p 71061 M